Chapter 13

Heat Transfer of Helix Energy Pile: Part 2—Novel Truncated Cone Helix Energy Pile

Guangqin Huang, Yajiao Liu, Xiaofeng Yang and Chunlong Zhuang

Additional information is available at the end of the chapter

http://dx.doi.org/10.5772/intechopen.76821

Abstract

Owing to the fact that severe thermal interferences exist in the radial and generatrix directions of the traditional cylinder helix energy pile due to the limited thermal heat capacity of the pile and small ratio between coil pitch and radius of pile, therefore, a novel truncated cone helix energy pile (CoHEP) is presented to weaken the thermal interferences and improve the heat transfer efficiency. Further, both the analytical solution model and numerical solution model for CoHEP are built to discuss the dynamic characteristics of thermal interferences and heat transfer performance. The results indicate that the thermal interference of CoHEP is dynamic. The thermal interference in the upper part of the CoHEP is much smaller than the traditional CyHEP. And in general the heat flux per unit pipe length of the novel CoHEP is larger than that of the traditional CyHEP. Heat flux per unit pipe length of the CoHEP increases linearly with inlet water temperature. For the same inlet water temperature, the thermal short circuit is serious at the bottom of the CoHEP, and it's weak in the upper part of CoHEP. Also it's obvious that as the inlet water temperature increases, the thermal short circuit becomes more serious.

Keywords: truncated cone, helix energy pile, analytical, numerical, thermal interferences, stages

1. Introduction

Although the CyHEP has the characteristics of large heat transfer area and large heat transfer, the results of Park et al. [1, 2] show that the traditional CyHEP has a close distance between the

adjacent tubes axially, which lead to a serious thermal interference phenomenon. Even when the pitch is small enough, the relative heat transfer efficiency is lower than the U-type ground heat exchanger. In addition, Yang et al. [3] conducted a laboratory investigation of the traditional CyHEP and found that the reduction in pitch would increase the total heat transfer but reduce the unit length of heat transfer. Thus it can be speculated that the distance between the adjacent tubes axially determines the thermal interference of the exchanger which plays an important role in the heat transfer efficiency. It can be found that at present researchers mainly study the mathematical models of the traditional CyHEP; there is little work about the thermal interference and heat transfer characteristics. Thus, in this section, for the sake of reducing thermal interference and improving heat transfer efficiency, a novel truncated cone helix energy pile (CoHEP) was proposed as shown in **Figure 1**.

As shown in **Figure 2**, the structure of novel CoHEP is characterized by the fact that the spiral heat transfer tube is wound on the wall of the truncated cone, and its spiral radius decreases linearly with the increase of the depth. **Figure 2** shows the physical mode of CoHEP. The cone angle is θ, the pitch in the depth direction is b, the distance between the adjacent tube is d; thus, the relationship between b and d is: $b = d \cdot \cos\theta$. What's more, the bottom radius is r_b, the top radius is r_t, $r_t > r_b$. The distance from the top of the structure to the ground surface is h_t and the distance from the bottom of the structure to the ground surface is h_b. And the spiral heat transfer tube is distributed according to the following equation:

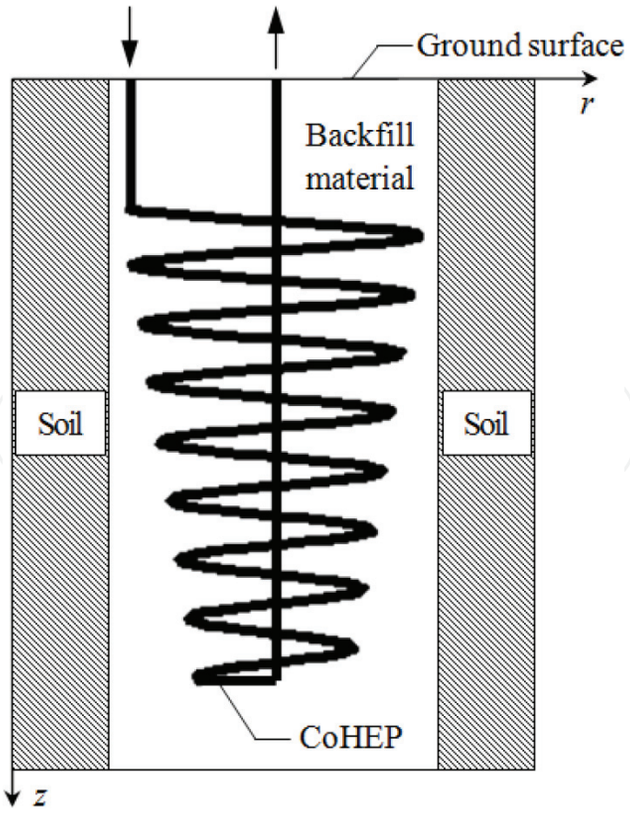

Figure 1. Truncated cone helix energy pile (CoHEP).

http://dx.doi.org/10.5772/intechopen.76821

$$\begin{cases} r = [r_b + (h_b - z) \cdot \tan\theta] \\ z = b \cdot \varphi/2\pi \end{cases} \quad (1)$$

where (r, ϕ, z) is the coordinate of a certain point of the truncated cone spiral coil structure in the column coordinate system.

Compared with the traditional CyHEP, the novel CoHEP proposed in this chapter has the following advantages:

1. Due to the fact that the spiral heat transfer tube of the novel CoHEP is wound on the wall of the truncated cone, there is a certain angle between the generatrix of the truncated cone and the vertical direction. Compared with the vertical generatrix of the cylinder, this can effectively reduce the risk of drilling wall collapse during construction.
2. When the fluid enters the heat transfer tube, the temperature difference between the top fluid and the soil is large and the radial thermal interference is strong which will weaken the heat transfer efficiency. Therefore, the novel CoHEP is designed with a larger top radius compared with the traditional CyHEP. This will effectively alleviate the radial thermal interference and improve thermal efficiency.
3. In the case where the pitch in the depth direction (b) is the same, the distance between the adjacent tube of CoHEP (d) can be calculated as: $d = b/\cos\theta$, which is obviously larger than the distance between the adjacent tube of CyHEP (b). It can effectively reduce the axial thermal interference and improve heat transfer efficiency.

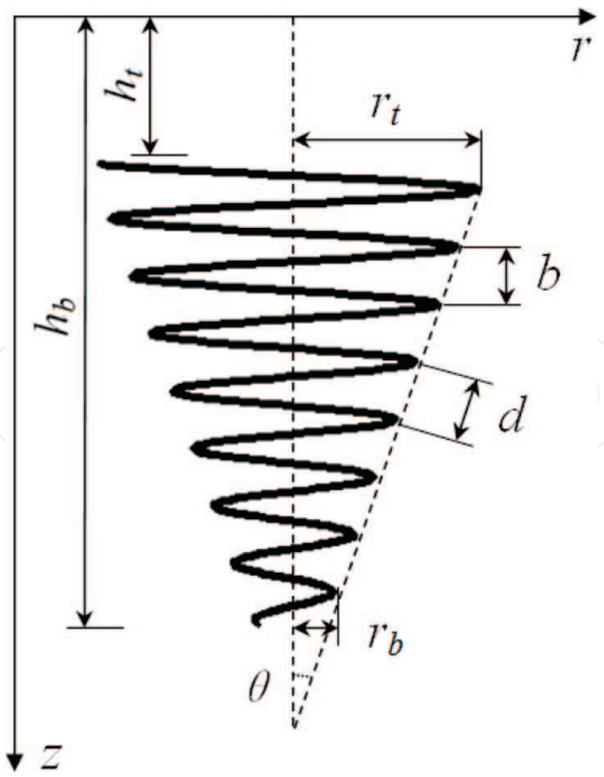

Figure 2. Structure of the novel CoHEP.

2. Heat transfer model and characteristics of the novel truncated cone helix energy pile (CoHEP)

2.1. Analytic solution model of CoHEP

2.1.1. Analytic solution model

To investigate the thermal performance of CoHEP, an analytical solution model of CoHEP based on Green's function is presented and the thermal interference of CoHEP is investigated in the manuscript.

For modeling the heat transfer of CoHEP, the following assumptions are made:

1. The medium is assumed to be a homogeneous infinite medium and the difference between soil and pile is ignored. The medium thermal properties do not change with the variation of temperature.
2. The medium has a uniform initial temperature, T_0.
3. The ground surface at $z = 0$ maintains a constant temperature, T_0.
4. Helix tube is regarded as a concentric spiral coil line with heating rate per length of pipe as ql. Mass, heat capacity, and thickness of the spiral coils' heat source are neglected.

The method of images for conduction questions is employed to maintain a constant temperature at the ground surface $z = 0$. Imagine that a mirror-image truncated cone spiral line of heat sink exists with heat rate $-q_l$, as shown in **Figure 3**.

On the condition of the above assumptions, the Green's function in the cylindrical coordinates could be written as Eq. (2) in the infinite medium. The Green's function represents the temperature rise by effect of an instantaneous point heat source of unit strength generated at time τ′ and at point (r', ϕ', z').

$$G\left(r^{'},,\varphi^{'},,z^{'},r,\varphi,z,,\tau^{'},\tau\right)=\frac{1}{8\left[\sqrt{\pi\alpha_s(\tau-\tau^{'})}\right]^3}\exp\left[-\frac{r^2+r'^2-2rr^{'}\cos\left(\varphi-\varphi^{'}\right)+\left(z-z^{'}\right)^2}{4\alpha_s(\tau-\tau^{'})}\right] \quad (2)$$

where G is the Green's function; α_s is the thermal diffusivity; τ' and τ is the time when heat is first emitted and the calculated time, respectively; (r', ϕ', z') are the heat sources or sink-point coordinates; (r, ϕ, z) are the coordinates at the calculated point in the medium except the heat source. In fact, the term of $r^2 + r'^2$-$2rr'\cos(\phi$-$\phi')$ + $(zi{-}z')^2$ is the square of distance from the calculated point to the point in the line of truncated cone spiral heat source or sink.

Based on the information given in **Figure 2**, the relationship among r', ϕ', z' would be described as Eq. (3) for truncated cone spiral heat source line with heat flux q_l:

$$\begin{cases} r^{'}=\left[r_{\mathrm{mi}}+\left(h_{\mathrm{mi}}-b\varphi^{'}/2\pi\right)\cdot\ \mathrm{tg}\,\theta\right] \\ z^{'}=b\varphi^{'}/2\pi \end{cases} \quad (3)$$

http://dx.doi.org/10.5772/intechopen.76821

Similarly, the relationship among coordinates of the mirror-image truncated cone spiral line of heat sinks is written as Eq. (4).

$$\begin{cases} r' = \left[r_{\mathrm{mi}} + \left(h_{\mathrm{mi}} - b\varphi'/2\pi\right) \cdot \mathrm{tg}\,\theta\right] \\ z' = -b\varphi'/2\pi \end{cases} \tag{4}$$

Hence, the distance dp from the heat source point (r', ϕ', z') to the calculated point (r, ϕ, z) could be described as Eq. (5) based on Eq. (3) and Eq. (4).

$$d_{\mathrm{p}} = \sqrt{\begin{array}{l} r^2 + \left[r_{\mathrm{mi}} + \left(h_{\mathrm{mi}} - b\varphi'/2\pi\right) \cdot \mathrm{tg}\,\theta\right]^2 - 2r\left[r_{\mathrm{mi}} + \left(h_{\mathrm{mi}} - b\varphi'/2\pi\right) \cdot \mathrm{tg}\,\theta\right] \\ \times\cos\left(\varphi - \varphi'\right) + \left(z - b\varphi'/2\pi\right)^2 \end{array}} \tag{5}$$

Accordingly, the distance dn from the heat sink point to the calculated point could be written as Eq. (6).

$$d_{\mathrm{n}} = \sqrt{\begin{array}{l} r^2 + \left[r_{\mathrm{mi}} + \left(h_{\mathrm{mi}} - b\varphi'/2\pi\right) \cdot \mathrm{tg}\,\theta\right]^2 - 2r\left[r_{\mathrm{mi}} + \left(h_{\mathrm{mi}} - b\varphi'/2\pi\right) \cdot \mathrm{tg}\,\theta\right] \\ \times\cos\left(\varphi - \varphi'\right) + \left(z + b\varphi'/2\pi\right)^2 \end{array}} \tag{6}$$

The temperature rise in the heat transfer medium is induced by the effects of spiral heat source and heat sink. Therefore, when the CoHEP emits heat at the intensity of q_l from time $\tau' = 0$, the

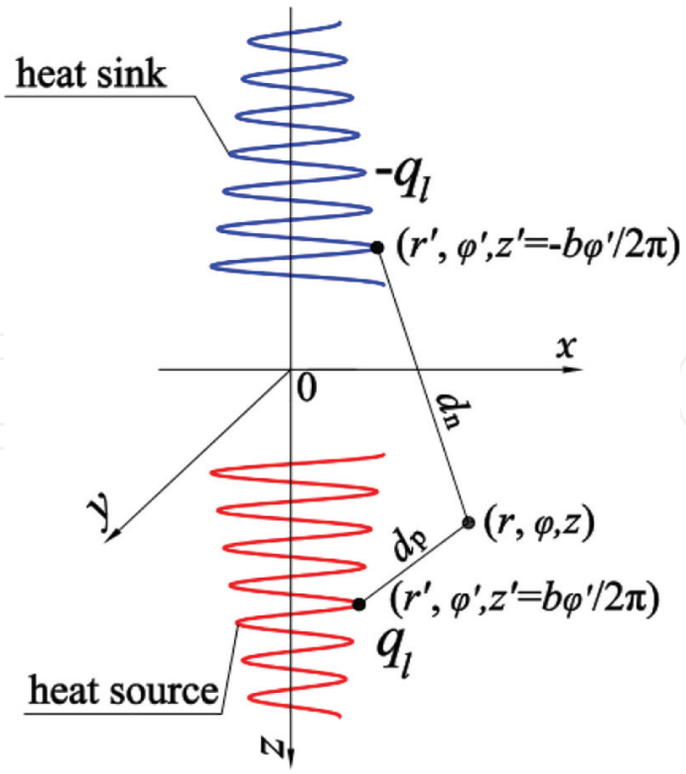

Figure 3. Schematic diagram of mirror heat source method.

temperature rise Δt can be obtained by integrating Green's function Eq. (2) with respect to the time τ' and the spiral line of heat source and sink.

$$\begin{aligned}\Delta T(r,\varphi,z,\tau) &= \frac{q_l}{\rho c}\int_0^{\tau}\int_L G\left(r',\varphi' z' = b\varphi'/2\pi r\varphi z,\tau'\tau\right) - G\left(r',\varphi' z' = -b\varphi'/2\pi r\varphi z,\tau'\tau\right)\mathrm{d}\tau\mathrm{d}l \\ &= \frac{q_l}{\rho c}\int_0^{\tau}\frac{1}{8\left[\sqrt{\pi\alpha_s(\tau-\tau')}\right]^3}\mathrm{d}\tau'\int_L\left\{\exp\left[-\frac{{d_p}^2}{4\alpha_s(\tau-\tau')}\right]-\exp\left[-\frac{{d_n}^2}{4\alpha_s(\tau-\tau')}\right]\right\}\mathrm{d}l\end{aligned} \tag{7}$$

where $\triangle T$ is the temperature rise; ρ is the density; c is the specific heat; L stands for the spiral line; and d_p and d_n are the above-defined ones.

Denoting $u = 1/\left[2\sqrt{\alpha_s(\tau-\tau')}\right]$ to make Eq. (7) concise, τ' is a function of u:

$$\tau' = \tau - 1/\left(4\alpha_s u^2\right) \tag{8}$$

Differential form of Eq. (8) would be achieved:

$$\mathrm{d}\tau' = 1/\left(2\alpha_s u^3\right)\mathrm{d}u \tag{9}$$

Thus, $u = 1/\left(2\sqrt{\alpha_s\tau}\right)$ when $\tau' = 0$ and $u = \infty$ when $\tau' = \tau$. Then, Eq. (7) can be transformed into another expression as follows.

$$\Delta T(r,\varphi,z,\tau) = \frac{q_l}{2\pi^{3/2}\lambda}\int_{1/(2\sqrt{\alpha\tau})}^{\infty}\mathrm{d}u\int_L\left\{\exp\left[-{d_p}^2u^2\right]-\exp\left[-{d_n}^2u^2\right]\right\}\mathrm{d}l \tag{10}$$

where λ is the thermal conductivity.

Eq. (10) is an expression of integrating with respect to the spiral coil line and is improper for computation. Thus, the transformation from the integration variable l to spiral angle ϕ' is necessary. The expression of the truncated cone spiral coil line in the Cartesian coordinates can be written as Eq. (11).

$$\begin{cases} x = \left[r_{mi} + \left(h_{mi} - b\varphi'/2\pi\right)\cdot\ \mathrm{tg}\,\theta\right]\cos\varphi' \\ y = \left[r_{mi} + \left(h_{mi} - b\varphi'/2\pi\right)\cdot\ \mathrm{tg}\,\theta\right]\sin\varphi' \\ z = \pm b/2\pi \end{cases} \tag{11}$$

Thus, the differential dl can be calculated by Eq. (12).

$$\mathrm{d}l = \sqrt{\mathrm{d}x^2+\mathrm{d}y^2+\mathrm{d}z^2} = \sqrt{\begin{matrix}\left[r_{mi} + \left(h_{mi} - b\varphi'/2\pi\right)\cdot\ \mathrm{tg}\,\theta\right]^2 \\ +b^2/4\pi^2\left(1+\left(\mathrm{tg}\,\theta\right)^2\right)\end{matrix}}\,\mathrm{d}\varphi' \tag{12}$$

Denoting $f(\varphi') = \sqrt{\left[r_{mi} + \left(h_{mi} - b\varphi'/2\pi\right)\cdot\ \mathrm{tg}\,\theta\right]^2 + b^2/4\pi^2(1+\ \mathrm{tg}\,\theta^2)}$ and then $\mathrm{d}l = f(\varphi')\mathrm{d}\varphi'$, Eq. (10) can be converted to Eq. (13).

$$\Delta T(r,\varphi,z,\tau)=\frac{q_l}{2\pi^{3/2}\lambda}\int_{2\pi h_t/b}^{2\pi h_b/b} f(\varphi')\mathrm{d}\varphi'\int_{1/(2\sqrt{\alpha\tau})}^{\infty}\left\{\exp\left[-{d_\mathrm{p}}^2u^2\right]-\exp\left[-{d_\mathrm{n}}^2u^2\right]\right\}\mathrm{d}u \tag{13}$$

Denoting $d_\mathrm{p}u=x_\mathrm{p}$ and $d_\mathrm{n}u=x_\mathrm{n}$, Eq. (14) can be obtained.

$$\Delta T(r,\varphi,z,\tau)=\frac{q_l}{2\pi^{3/2}\lambda}\int_{2\pi h_t/b}^{2\pi h_b/b} f(\varphi')\mathrm{d}\varphi'\left\{\begin{array}{l}\dfrac{1}{d_\mathrm{p}}\cdot\displaystyle\int_{d_\mathrm{p}/\left(2\sqrt{\alpha_\mathrm{s}\tau}\right)}^{\infty}\exp\left[-{x_\mathrm{p}}^2\right]\mathrm{d}x_\mathrm{p}\\ -\dfrac{1}{d_\mathrm{n}}\cdot\displaystyle\int_{d_\mathrm{n}/\left(2\sqrt{\alpha_\mathrm{s}\tau}\right)}^{\infty}\exp\left[-{x_\mathrm{n}}^2\right]\mathrm{d}x_\mathrm{n}\end{array}\right\} \tag{14}$$

According to the characteristics of the error function, the more concise expression can be achieved.

$$\Delta T(r,\varphi,z,\tau)=\frac{q_l}{4\pi\lambda}\int_{2\pi h_t/b}^{2\pi h_b/b} f(\varphi')\left[\frac{1}{d_\mathrm{p}}\cdot\mathrm{erfc}\left(\frac{d_\mathrm{p}}{2\sqrt{\alpha_\mathrm{s}\tau}}\right)-\frac{1}{d_\mathrm{n}}\cdot\mathrm{erfc}\left(\frac{d_\mathrm{n}}{2\sqrt{\alpha_\mathrm{s}\tau}}\right)\right]\mathrm{d}\varphi' \tag{15}$$

In which, $\mathrm{erfc}(x)=1-\frac{2}{\sqrt{\pi}}\int_0^x\exp\left(-u^2\right)\mathrm{d}u$ is the complementary error function. The final analytical solution of CoHEP can be obtained by employing $f(\phi')$ into Eq. (15).

$$\Delta T(r,\varphi,z,\tau)=\frac{q_l}{4\pi\lambda}\int_{2\pi h_t/b}^{2\pi h_b/b}\sqrt{\left[r_\mathrm{mi}+\left(h_\mathrm{mi}-\frac{b\varphi'}{2\pi}\right)\cdot\mathrm{tg}\,\theta\right]^2+\frac{b^2}{4\pi^2}\left(1+(\mathrm{tg}\,\theta)^2\right)}\left[\begin{array}{l}\dfrac{1}{d_\mathrm{p}}\cdot\mathrm{erfc}\left(\dfrac{d_\mathrm{p}}{2\sqrt{\alpha_\mathrm{s}\tau}}\right)\\ -\dfrac{1}{d_\mathrm{n}}\cdot\mathrm{erfc}\left(\dfrac{d_\mathrm{n}}{2\sqrt{\alpha_\mathrm{s}\tau}}\right)\end{array}\right]\mathrm{d}\varphi' \tag{16}$$

To reduce the number of parameters and simplify the calculation, the corresponding non-dimensional parameters should be denoted: $\Theta=\lambda\triangle T/q_l$, $H_{mi}=h_{mi}/r_{mi}$, $B=b/r_{mi}$, $R=r/r_{mi}$, $R_b=r_b/r_{mi}$, $Z=z/r_{mi}$, $Fo=\alpha_s\tau/{r_{mi}}^2$. Thus, the dimensionless expression of CoHEP can be obtained:

$$\Theta=\frac{1}{4\pi}\int_{2\pi H_t/B}^{2\pi H_b/B}\sqrt{\left[1+\left(H_\mathrm{mi}-\frac{B\varphi'}{2\pi}\right)\cdot\mathrm{tg}\,\theta\right]^2+\frac{B^2}{4\pi^2}(1+\mathrm{tg}\,\theta^2)}\cdot\left[\begin{array}{l}\dfrac{1}{D_\mathrm{p}}\cdot\mathrm{erfc}\left(\dfrac{D_\mathrm{p}}{2\sqrt{Fo}}\right)\\ -\dfrac{1}{D_\mathrm{n}}\cdot\mathrm{erfc}\left(\dfrac{D_\mathrm{n}}{2\sqrt{Fo}}\right)\end{array}\right]\mathrm{d}\varphi' \tag{17}$$

In which

$$D_\mathrm{p}=\sqrt{R^2+\left[1+(H_\mathrm{mi}-B\varphi'/2\pi)\cdot\mathrm{tg}\,\theta\right]^2-2R\left[1+(H_\mathrm{mi}-B\varphi'/2\pi)\cdot\mathrm{tg}\,\theta\right]\cos(\varphi-\varphi')+(Z-B\varphi'/2\pi)^2}$$

$$D_\mathrm{n}=\sqrt{R^2+\left[1+(H_\mathrm{mi}-B\varphi'/2\pi)\cdot\mathrm{tg}\,\theta\right]^2-2R\left[1+(H_\mathrm{mi}-B\varphi'/2\pi)\cdot\mathrm{tg}\,\theta\right]\cos(\varphi-\varphi')+(Z+B\varphi'/2\pi)^2}$$

In fact, the dimensionless expression Eq. (17) will become Eq. (18) when the cone angle θ equals to zero. Further, we found that the form of Eq. (18) is also the analytical solution of ScM [4, 5], which is indicated that the ScM is a particular case of the CoHEP model presented in the section.

$$\Theta = \frac{1}{4\pi}\int_{2\pi H_t/B}^{2\pi H_b/B}\sqrt{1+\frac{B^2}{4\pi^2}}\cdot\left[\frac{1}{D_\mathrm{p}}\cdot\mathrm{erfc}\left(\frac{D_\mathrm{p}}{2\sqrt{Fo}}\right)-\frac{1}{D_\mathrm{n}}\cdot\mathrm{erfc}\left(\frac{D_\mathrm{n}}{2\sqrt{Fo}}\right)\right]\mathrm{d}\varphi' \tag{18}$$

In which

$$D_\mathrm{p} = \sqrt{R^2+1-2R\cos(\varphi-\varphi')+(Z-B\varphi'/2\pi)^2}$$

$$D_\mathrm{n} = \sqrt{R^2+1-2R\cos(\varphi-\varphi')+(Z+B\varphi'/2\pi)^2}$$

The term of $\sqrt{1+B^2/4\pi^2}$ in Eq. (18) is induced by the different definitions of heating rate q_l in the ScM and the proposed model in the manuscript. The ScM treats the ql as heating rate per depth of pile while the ql is regarded as heating rate per length of pipe in the model of CoHEP.

2.1.2. Calculation of pipe wall temperature rise

The temperature rise on the pipe wall is an important parameter and could reflect the heat transfer characteristic of CoHEP, which also directly affects the energy efficiency of GSHP systems. To calculate the average temperature on the pipe wall accurately, the helical pipe is divided into numbers of spiral arc sections, and the number of spiral sections is n, the length of each spiral section is L_j, as shown in **Figure 4**. According to Eq. (11), $L_j = f(\phi_j)\cdot\triangle\phi_j$. Therefore, the entire pipe wall's dimensionless temperature rise Θ_{ave} can be obtained by the way of weighted average among the spiral arc sections as Eq. (19).

$$\Theta_\mathrm{ave} = \frac{\sum_{j=1}^{n} L_j\Theta_{\mathrm{ave},j}}{\sum_{j}^{n} L_j} = \frac{\sum_{j=1}^{n} f(\varphi_j)\Delta\varphi_j\Theta_{\mathrm{ave},j}}{\sum_{j}^{n} f(\varphi_j)\Delta\varphi_j} \tag{19}$$

where ϕ_j and $\triangle\phi_j$ is the spiral angle and increment of spiral angle, respectively and $\Theta_{ave,j}$ is the average dimensionless temperature rise of the jth spiral section of helical pipe.

The cross-section of pipe with a radius of r_s is divided into four circular arcs to meet the demands of accuracy and the value of angle for each circular arc is $\pi/2$. So the average temperature raise of the jth spiral section of helical pipe can be determined:

$$\Theta_{\mathrm{ave},j} = \sum_{i=1}^{4}\Theta_i/4 \tag{20}$$

where i stands for the index of the divided circular arc.

Ultimately, the influence coefficient η is employed to discuss the heat transfer efficiency of CoHEP compared with CyHEP, quantitatively.

$$\eta = \left(\frac{1}{\Theta_{\text{ave, CoHEP}}} - \frac{1}{\Theta_{\text{ave, CyHEP}}}\right) / \frac{1}{\Theta_{\text{ave, CyHEP}}} \tag{21}$$

It's known that Θ_{ave} could stand for the thermal resistance of the ground. Therefore, the reciprocal of Θ_{ave} can be the representative for the heat transfer coefficient. Hence, the employed influence coefficient η can reflect the thermal performance of CoHEP, especially for analysis of the influence of cone angle on heat transfer.

2.2. Numerical solution model of CoHEP

As the geometry of CoHEP is complex, the three-dimensional model of prototype is too complex and difficult to calculate. In order to improve the efficiency of simulation calculation, a laboratory-scale model was built based on the similarity principle. This will help achieve a long-term simulation of CoHEP efficiently, with lower computer configuration requirements and also a shorter calculation cycle. Innovatively, in addition to calculating the temperature of outlet water and the measuring point in the soil, the temperature of the fluid along the spiral tube is also calculated in order to study the heat transfer characteristics along the novel CoHEP.

2.2.1. CoHEP model

Similarity principle was used to shrink the prototype model in this chapter. According to the similarity principle, the similarity index of two similar models must be equal to 1 for the sake of thermal performance of the prototype and miniature models. When the miniature model of

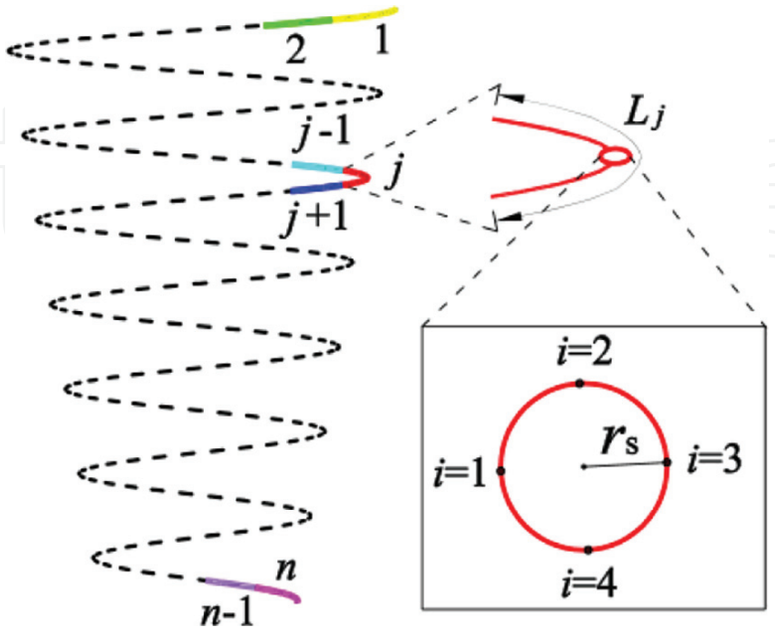

Figure 4. Schematic diagram of calculation of entire average temperature rise on the wall of pipe.

the CoHEP was designed, the heat transfer model was similarly converted using the length-scale coefficient on the prototype basis, and the soil physical parameters and the fluid in the miniature model were the same as the prototype one. Thus, according to the theory of heat transfer similarity, the Nu, Fo, and Re numbers in the prototype and miniature models were equal. Under the conditions set above, the relationship between the calculation time of the miniature and prototype system is that:

$$\tau_{min} = C_l^2 \cdot \tau_{pro} \tag{22}$$

Therefore, by scaling the prototype model the calculation results can be obtained in a relatively short period of time comparing the long-time calculation cycle of the prototype model. And it will certainly reduce the requirements for computer configuration. Through the analysis above, we can get the corresponding parameters of the prototype and miniature models, and they are shown in **Table 1**.

An example of the novel CoHEP whose θ is 10° is given in **Figure 5**. The detailed dimensions are shown in the figure. In this chapter the model was built by Solidworks, and imported to

Parameters	Spiral pitch in the depth direction/m	Bottom diameter/m	Inside diameter of coil pipe/m	Total length/m	Water flow/L/h	Time/h	Re
Prototype	0.17	0.5	0.025	100	175	300	3611
Miniature	0.034	0.1	0.005	20	35	12	3611

Table 1. The main parameters for the miniature and prototype models.

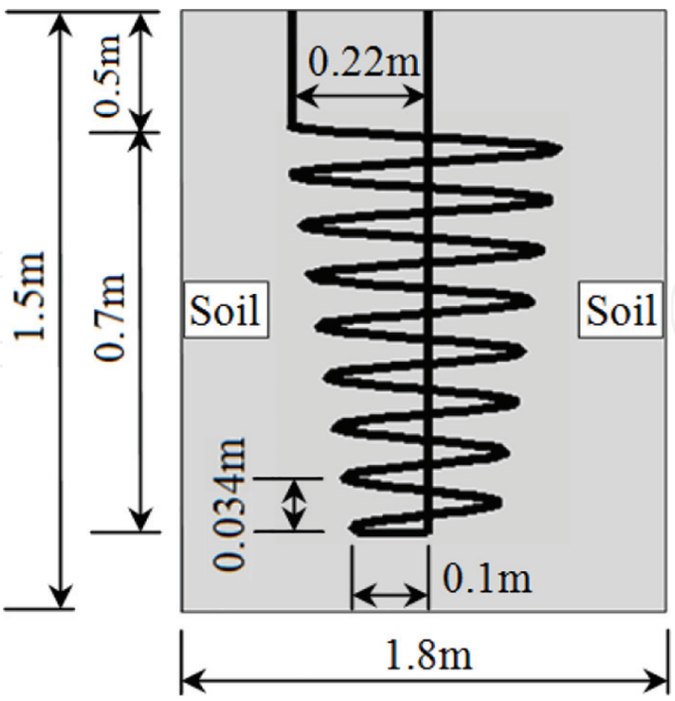

Figure 5. CoHEP of 10° cone angle.

http://dx.doi.org/10.5772/intechopen.76821

Workbench for grid partitioning. The three-dimensional unstructured grid and CoHEP positioning are shown in **Figure 6**. As the temperature change around the spiral tube is more intense and the calculation accuracy requirement is higher, the grid around the tube is partially encrypted. At the same time, the soil temperature changes more and more slowly as the radius increases, so the spacing of the grid can be increased in the radial direction. What's more, owing to the fact that the inlet and outlet sections of the CoHEP are wrapped in insulation material, there is no heat exchange in those sections. Thus for the convenience of grid partitioning, the outlet section was moved from the center of the CoHEP to the bottom of the model when the model was built. In the simulation process, three sets of different grids (3,233,475, 3,907,586, 4,590,437) for the same geometric model were built, respectively. By comparison, the increase in the number of grids results in almost no effect on the calculation results. Thus the grid number of 3,233,475 was selected as the computational grid of the model. The main parameters of the numerical model are listed in **Table 2** that are obtained from the verification test.

2.2.2. Governing equations

As for the ground heat exchanger, fluid in the pipe relies on the pump for forced circulation, so it's the forced convection heat transfer between the fluid and pipe wall. In this chapter, soil is treated as homogeneous and isotropic solid and the effect of groundwater seepage is ignored; thus, there is only thermal conductivity in the soil.

In the simulation, the k-ε two-equation model is chosen for the flow of the fluid in the CoHEP. The general form of the governing equations is shown below:

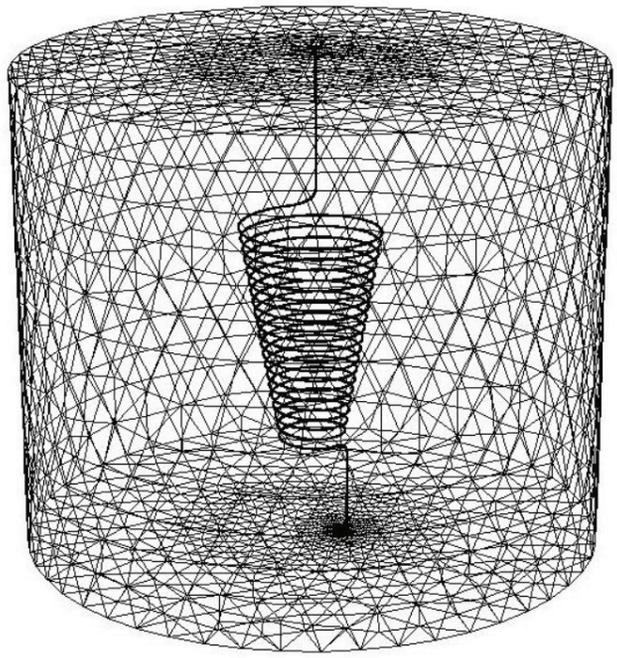

Figure 6. 3-D unstructured grid of CoHEP.

Parameter	Component	Symbol	Value	Unit
Density	Water	ρ_f	993.45	kg/m^3
	Pipe	ρ_p	900	kg/m^3
	Soil	ρ_s	2500	kg/m^3
Heat conductivity	Water	λ_f	0.72	W/(m·K)
	Pipe	λ_p	0.35	W/(m·K)
	Soil	λ_s	0.4	W/(m·K)
Gravimetric heat capacity	Water	c_f	4182	J/(kg·K)
	Pipe	c_p	1920	J/(kg·K)
	Soil	c_s	920	J/(kg·K)
Inlet water temperature	Water	T_{in}	38	°C
Water flow rate	Water	V_f	35	L/h

Table 2. The main parameters of the numerical model.

$$\frac{\partial\left(\rho_f\phi\right)}{\partial\tau}+\frac{\partial\left(\rho_f u\phi\right)}{\partial x}+\frac{\partial\left(\rho_f v\phi\right)}{\partial y}+\frac{\partial\left(\rho_f w\phi\right)}{\partial z}=\frac{\partial}{\partial x}\left(\Gamma\frac{\partial\phi}{\partial x}\right)+\frac{\partial}{\partial y}\left(\Gamma\frac{\partial\phi}{\partial y}\right)+\frac{\partial}{\partial z}\left(\Gamma\frac{\partial\phi}{\partial z}\right)+S \quad (23)$$

$$\frac{\partial\left(\rho_f\phi\right)}{\partial\tau}+\mathrm{div}\left(\rho_f\,\vec{V}\,\phi\right)=\mathrm{div}\left(\Gamma\ \cdot\ \mathrm{grad}\left(\phi\right)\right)+S \quad (24)$$

Table 3 lists the governing equations for the k-ε two-equation model in the Cartesian coordinate system, and the turbulent kinetic energy generation term G_k from the mean velocity gradient is:

$$G_k=\frac{\eta_t}{\rho_f}\left\{2\ \cdot\ \left[\left(\frac{\partial u}{\partial x}\right)^2+\left(\frac{\partial v}{\partial y}\right)^2+\left(\frac{\partial w}{\partial z}\right)^2\right]+\left(\frac{\partial u}{\partial y}+\frac{\partial v}{\partial x}\right)^2+\left(\frac{\partial u}{\partial z}+\frac{\partial w}{\partial x}\right)^2+\left(\frac{\partial v}{\partial z}+\frac{\partial w}{\partial y}\right)^2\right\} \quad (25)$$

where u, v, w, respectively, represents the velocity in the x, y, z direction in the Cartesian coordinate system. k is the turbulent kinetic energy. ε is the turbulent energy dissipation rate. η is the molecular viscosity coefficient. η_t is the turbulent viscosity coefficient. η_{eff} is the effective viscosity coefficient. σ_k, σ_ε, σ_T, respectively, represents the turbulent Prandtl number of the turbulent kinetic energy k, the turbulent kinetic energy dissipation rate ε, and the temperature T_f. ρ_f is the density of the fluid. P_f is the pressure of the fluid.

As soil is treated as homogeneous and isotropic solid and the effect of groundwater seepage is ignored, thus, there is only thermal conductivity in the soil. The thermal governing equation in the soil can be expressed by the following formula:

$$\frac{\partial(\rho_s T_s)}{\partial\tau}=\frac{\partial}{\partial x}\left(\frac{\lambda_s}{c_s}\ \cdot\ \frac{\partial T_s}{\partial x}\right)+\frac{\partial}{\partial y}\left(\frac{\lambda_s}{c_s}\ \cdot\ \frac{\partial T_s}{\partial y}\right)+\frac{\partial}{\partial z}\left(\frac{\lambda_s}{c_s}\ \cdot\ \frac{\partial T_s}{\partial z}\right) \quad (26)$$

Equation	ϕ	Γ	S
Continuity equation	1	0	0
X-momentum equation	u	$\eta_{eff} = \eta + \eta_t$	$-\frac{\partial p_f}{\partial x} + \frac{\partial}{\partial x}\left(\eta_{eff}\frac{\partial u}{\partial x}\right) + \frac{\partial}{\partial y}\left(\eta_{eff}\frac{\partial v}{\partial x}\right) + \frac{\partial}{\partial z}\left(\eta_{eff}\frac{\partial w}{\partial x}\right)$
Y-momentum equation	v	$\eta_{eff} = \eta + \eta_t$	$-\frac{\partial p_f}{\partial y} + \frac{\partial}{\partial x}\left(\eta_{eff}\frac{\partial u}{\partial y}\right) + \frac{\partial}{\partial y}\left(\eta_{eff}\frac{\partial v}{\partial y}\right) + \frac{\partial}{\partial z}\left(\eta_{eff}\frac{\partial w}{\partial y}\right)$
Z-momentum equation	w	$\eta_{eff} = \eta + \eta_t$	$-\frac{\partial p_f}{\partial z} + \frac{\partial}{\partial x}\left(\eta_{eff}\frac{\partial u}{\partial z}\right) + \frac{\partial}{\partial y}\left(\eta_{eff}\frac{\partial v}{\partial z}\right) + \frac{\partial}{\partial z}\left(\eta_{eff}\frac{\partial w}{\partial z}\right)$
Turbulent kinetic energy	k	$\eta + \frac{\eta_t}{\sigma_k}$	$\rho_f G_k - \rho_f \varepsilon$
Turbulence energy dissipation rate	ε	$\eta + \frac{\eta_t}{\sigma_\varepsilon}$	$\frac{\varepsilon}{k}\left(c_1\rho_f G_k - c_2\rho_f \varepsilon\right)$
Energy equation	T	$\frac{\eta}{\mathrm{Pr}} + \frac{\eta_t}{\sigma_T}$	0

Table 3. The governing equations for the k-ε two-equation model in the Cartesian coordinate system.

where c_s is the specific heat capacity of the soil. λ_s is the thermal conductivity of the soil. T_s is the temperature.

2.2.3. Initial and boundary conditions

As the depth of the CyHEP is shallow, it's usually buried 10–20 m below from the surface of the ground. Thus the heat transfer of the buried pipe is greatly affected by the environmental conditions of the soil surface. Particularly, as the top diameter of the novel CoHEP is bigger than the traditional CyHEP, there is more area of pipe close to the ground surface. Thus the effects of dynamic surface conditions on the heat transfer of the novel CoHEP cannot be ignored. However, for the sake of computational convenience most models of the traditional CyHEP including the analytical solution models and the numerical solution models always make a certain simplification by setting the ground surface temperature as a constant one which will lead to the deviation from actual situation.

Figure 7 shows the dynamic near-surface air temperature recorded in the verification test. The following functional Eq. (27) is obtained by fitting the recorded data. And the corresponding fitting curve is shown in **Figure 5**.

$$\begin{cases} T_{air} = 24.3 - 0.026\tau + 3.3 \times 10^{-4}\tau^2 - 1.6 \times 10^{-6}\tau^3, 0 \le \tau \le 50 \\ T_{air} = 23.6 + 4.7 \times 10^{-4}\tau, \qquad\qquad 50 < \tau \le 720 \end{cases} \tag{27}$$

where T_{air} is the near-surface air temperature. τ is the system running minutes.

The initial soil temperature distribution is affected by air temperature and solar radiation, which varies with depth and time, and has a great influence on the heat transfer performance of underground tube heat exchangers. It's one of the most basic parameters in theoretical calculations. Especially for the CoHEP, due to its shallow depth, the initial soil temperature distribution is not uniform. Considering the initial soil temperature gradient in the depth direction, the model will be more suitable for the actual condition. **Figure 8** shows the initial soil temperature distribution in the depth direction recorded in the verification test. The

following functional Eq. (28) is obtained by fitting the recorded data. And the corresponding fitting curve is shown in **Figure 8**.

$$T_{initial} = 24.3 - 1.44h + 1.05h^2 - 0.27h^3 \tag{28}$$

where $T_{initial}$ is the initial soil temperature and h is the depth in the soil.

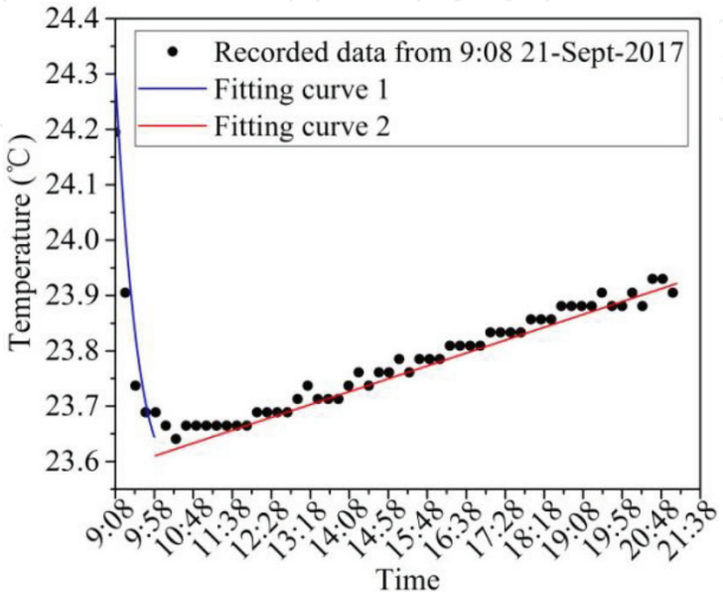

Figure 7. Recorded dynamic near-surface air temperature.

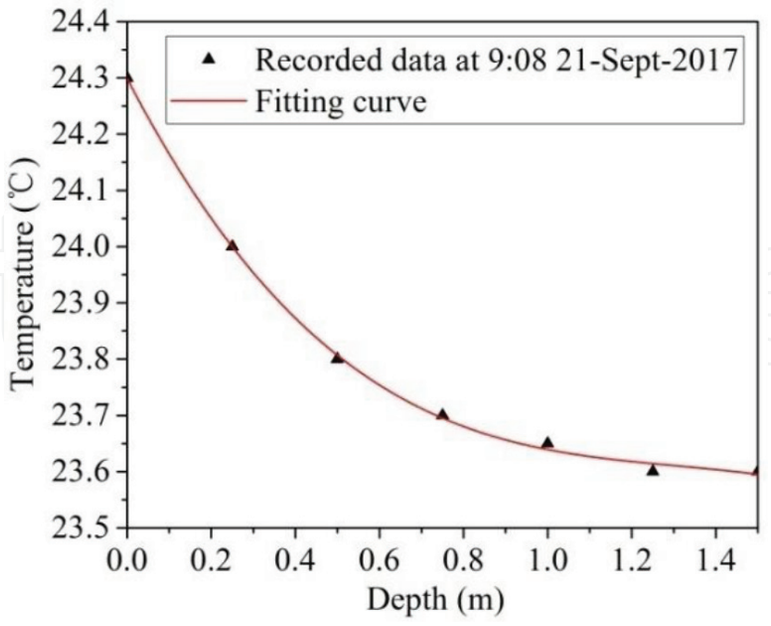

Figure 8. Recorded initial soil temperature distribution in the depth direction.

Both the dynamic surface condition and the initial soil temperature are modified with user defined functions (UDF) written in C language according to the functions above and then incorporated to the calculation model. As for the model's other boundary conditions, the top surface, bottom surface and the surrounding surface of the cylindrical soil model, are defined as the wall boundary. The inlet of the tube is set to velocity-flow-inlet and the outlet is set to pressure-outlet. Buried pipe and soil areas are solid; the area inside the tube is fluid.

2.2.4. CFD simulation setup

The commercial CFD software ANSYS_FLUENT is used to simulate the heat transfer of the CoHEP. Because the length of the tube is 20 m, the inside diameter of the tube is 0.005 m; thus, the model belongs to the slender region heat transfer model and the solver selected in the calculation is a three-dimensional double-precision solver. What's more, k-ε two-equation model is selected for calculating the turbulent flow in the tube. The physical parameters of fluid in the tube, buried pipe and soil areas are defined according to the verification test experiment. The top surface of the soil model is defined as the heat transfer boundary according to the actual situation. The bottom surface and surrounding surface of the cylindrical soil model are defined as adiabatic boundary conditions. The momentum equation, turbulent kinetic energy equation, turbulence energy dissipation rate and the energy equation all use the second-order upwind discretization format for calculation.

In order to help analyze the thermal performance of CoHEP, three-series monitoring points (a total of 18) shown in **Figure 9(a)** are set to monitor the soil temperature. Innovatively, a series of monitoring points are set along the tube of CoHEP to investigate the water temperature drop along the tube, and the separation distance of the points is shown in **Figure 9(b)**.

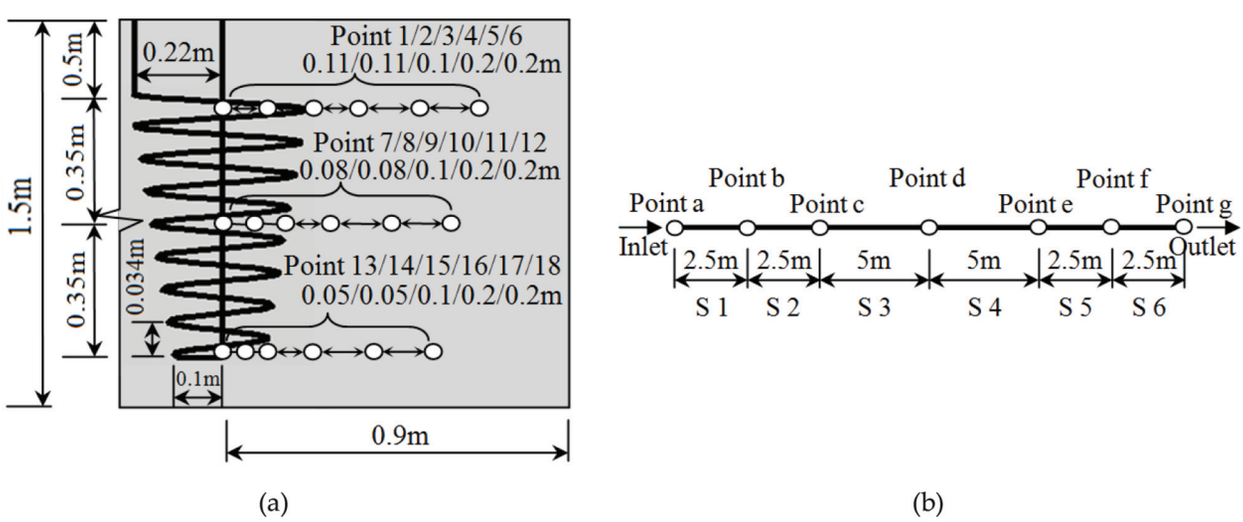

Figure 9. Arrangements of series monitoring points. (a) Monitoring points in the soil, (b) monitoring points in the pipe of CoHEP.

2.3. Heat transfer characteristics of CoHEP

2.3.1. The thermal interference of CoHEP by analytic solution model

Significant radial thermal interferences (RTI) and generatrix thermal interferences (GTI) exist in the cylinder helix energy pile. **Figure 10(a)** shows the contour of Θ in the Z-R plan of CyHEP with $\phi = 180°$, $B = 1$ and Fo = 10. It is indicated that GTI is serious duo to the small pitch and also RTI is significant because of the limited thermal heat capacity of pile, especially in the middle of pile. However, the remarkable 3-D effect weakens both RTI and GTI at the upper and lower part of pile, which leads to the reduction of Θ at the top and base of CyHEP compared to the middle of CyHEP.

The contours of Θ in the Z-R plan of CoHEP with $\theta = 5°$ and $\theta = 10°$ are shown as **Figure 10(b)** and **Figure 10(c)**, respectively, when the length of heat exchange pipe is consistent. The figures show that bigger the cone angle, lower the dimensionless temperature at the bottom of HEP. The upper part of CyHEP has the same situation. It is indicated that the structure of CoHEP can weaken the GTI in the bottom of pile due to the local large ratio between coil pitch and radius of pile. Besides, the degree of RTI also reduces in the upper parts of pile because of the local large radius.

2.3.2. The dynamic thermal interference of CoHEP by analytic solution model

The CoHEP can effectively reduce the thermal interference, and further investigations discover that the thermal interference is dynamic by analyzing the Z-Θ curve on the generatrix of

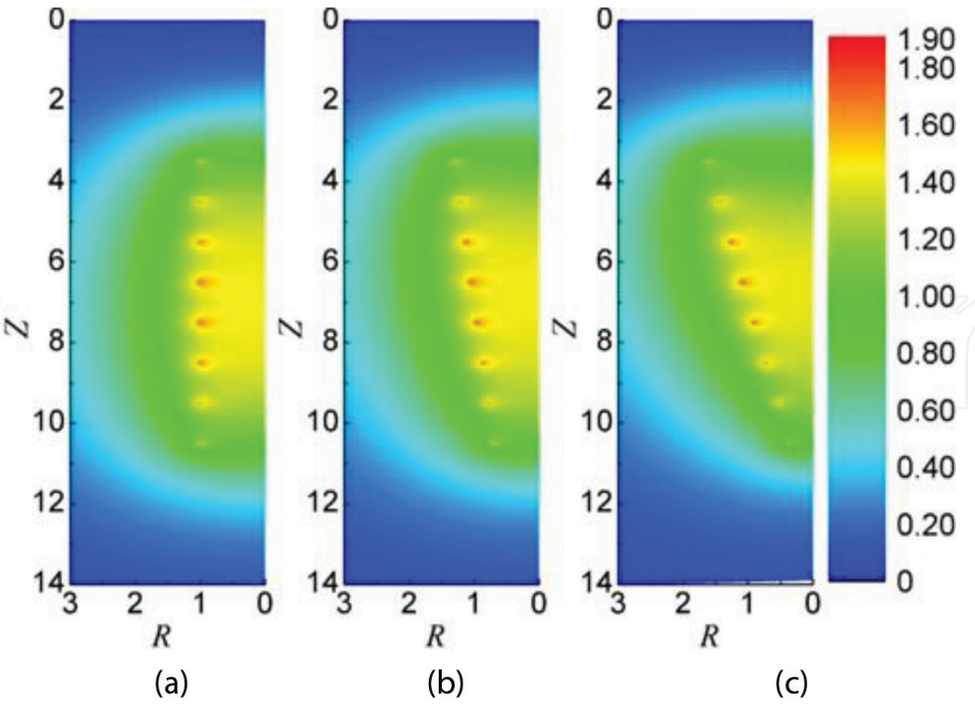

Figure 10. Contours of dimensionless temperature rise in the Z-R plan at $\phi = 180°$($B = 1$, Fo = 10). (a) $\theta = 0°$, (b) $\theta = 5°$, (c) $\theta = 10°$.

CyHEP and CoHEP with variable Fo from 0.01 to 100. The calculation precondition is that length of pipe and coil pitch are consistent. The results are shown in **Figure 11**.

With the increasing Fo, the ground surface boundary thermal interference (BTI) appears, in addition to the RTI and GTI. BTI is induced by the first kind of boundary condition and affected by distance from the top surface of CoHEP to the ground surface ht. Besides, according to the expression of Green's function, the heat affected zone is continuously growing with the increasing Fo, which results in the aggravation of three thermal interferences. However, each kind of thermal interference has a spatial inconsistence with variation of Fo.

In order to explain the dynamic characteristics revealed by the Z-Θ curve from Fo = 0.01 to Fo = 100 plotted in **Figure 11**, six different degrees are qualitatively defined to describe the thermal interference including "none," "little," "mild," "moderate," "serious," and "severe." The defined degree gradually increases from "none" to "severe." According to both the structure features of HEP and the plotted Z-Θ curve, the specific degrees of RTI, GTI, and BTI have been deduced, which has been noted at the top and bottom of figure for each case of Fo.

Figure 11 shows that Θ in the middle of the adjacent coils is zero when Fo is very small (such as Fo = 0.01), which indicates that the degrees of thermal interference are "none" and the curves of Z-Θ for CyHEP and CyHEP overlap. With the increase of Fo, RTI at the base of CoHEP appears firstly due to the small base radius when cone angle θ equals to 10° and then, the GTI in the CyHEP and the top of CoHEP begins to emerge because of the small ratio between coil pitch and local radius of pile. Next, the RTI in the CyHEP and the top of CoHEP tends to appear in succession due to the large radius of pile. Finally, BTI starts to show in the top of CyHEP and CoHEP due to the distance of ht. It is worth mentioning that the Θ in the top of HEP would be severely influenced by BTI when Fo is big (such as Fo = 10 and 100).

In general, the GTI in CoHEP tends to weaken with the increasing of depth, because the ratio between coils pitch and local radius of the pile gradually increases while the local radius of pile linearly decreases. Therefore, the GTI in the base of CoHEP is weaker than other place of CoHEP and CyHEP, and the dimensionless temperature rise Θ in the base of CoHEP is lower when Fo > 1. However, the Θ in the base is higher than that of CyHEP when Fo < 1 due to the local smaller radius of CoHEP, which means that the RTI of CyHEP is weaker than that of CoHEP in the base of the pile for a small Fo (such as Fo = 0.1 and Fo = 0.5).

Besides, the Θ in the top of CoHEP is lower than that of CyHEP with range of Fo from 0.1 to 5 due to a large local radius of CoHEP, which indicates that the RTI of CoHEP is weaker than that of CyHEP in the top of the pile. However, the curves in the top of CyHEP and CoHEP overlaps while Fo > 5 because the BTI tends to be severe.

2.3.3. Heat transfer characteristics of CoHEP by the numerical solution model

Ground source heat pump heat exchanger relies on the temperature difference between the circulating medium in the pipe and the soil around the pipe to absorb or release energy, thus heating or cooling the circulating medium in the pipe. The temperature of the circulating medium in the pipe has a significant effect on the heat transfer of the ground heat exchanger,

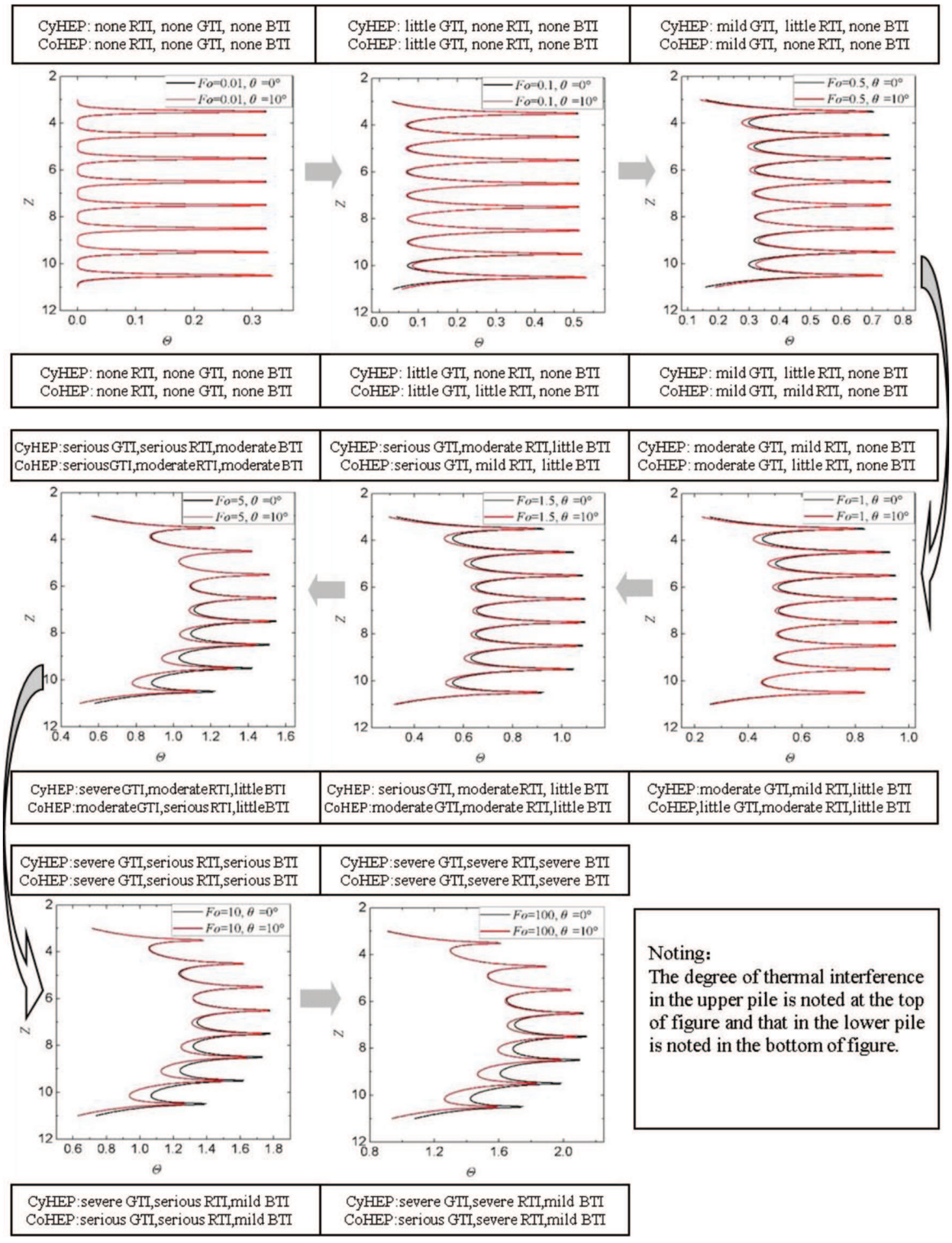

Figure 11. Dynamic characteristic of thermal interference of HEP ($B = 1$, $\phi = 180°$).

while the temperature of the circulating medium in the pipe is controlled by the inlet temperature of the ground heat exchanger.

In order to investigate the influence of inlet water temperature on the heat transfer performance of the novel CoHEP, three different inlet water temperatures, 33, 38, 43°C are chosen to study in this chapter. These three conditions are simulated with the established numerical model verified above. All the other parameters in addition to the inlet water temperature are the same as shown in **Table 2**.

Figure 12 shows the simulated outlet water temperature changing with operation time in three different inlet water temperature conditions. We can easily find that the outlet water temperature increases with time and eventually gradually reaches a steady state. Correspondingly, **Figure 13** shows the simulated heat flux per unit pipe length changing with operation time in these three conditions. And it shows that the heat flux per unit pipe length decreases with time and eventually reaches a steady state. The main reason for this trend is: In the early stage of operation, the temperature difference between the fluid and soil is large, and the heat transfer is sufficient. Therefore the system has large inlet and outlet water temperature difference and large heat transfer flux. However, after that, the heat-affected zone increases in radius and the thermal resistance of the soil becomes the main contradiction of the heat transfer process, resulting in the decrease of the heat transfer rate. After a period of heat exchange, with the heat accumulation in the soil, the temperature difference between the fluid and soil is small; thus, the heat flux per unit pipe length sharply reduces. And then later, when the soil temperature field tends to be stable, the heat transfer performance also is gradually stabilized. As shown in **Figure 14**, the heat flux per unit pipe length increases linearly as the inlet water temperature increases. When the system running time is 4, 8, and 12 h, respectively, the heat

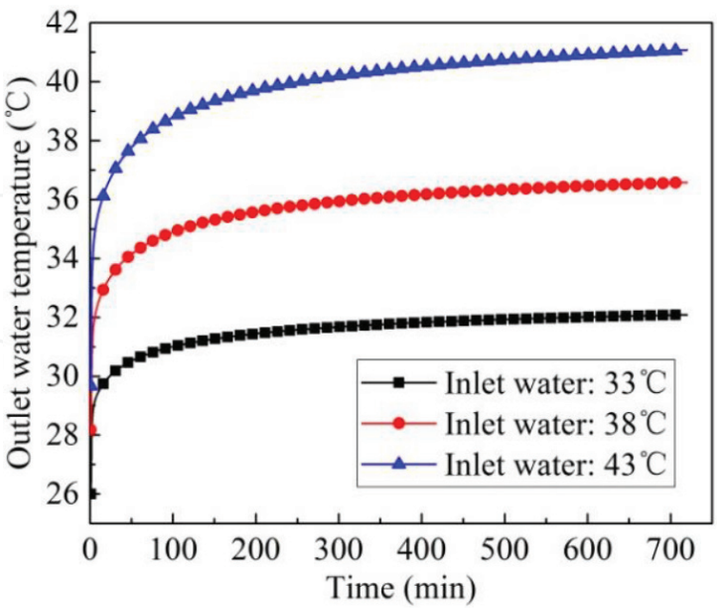

Figure 12. Outlet water temperature with operation time under different inlet water temperatures.

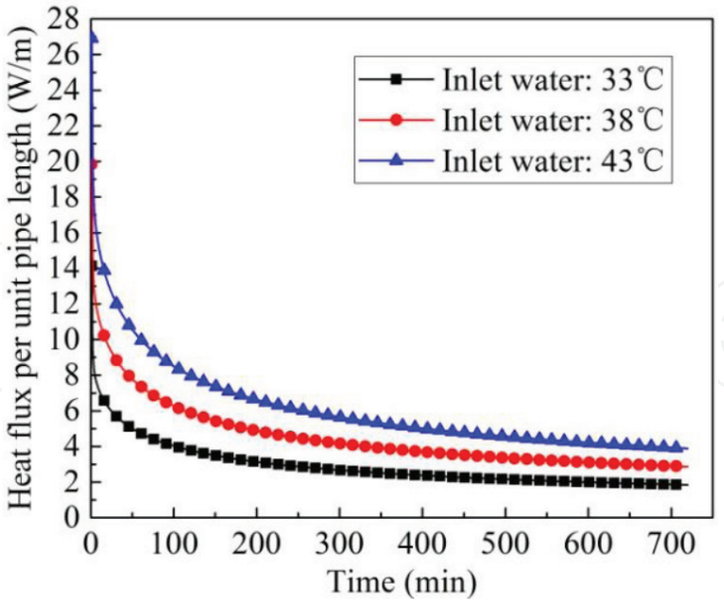

Figure 13. Heat flux per unit pipe length with operation time under different inlet water temperatures.

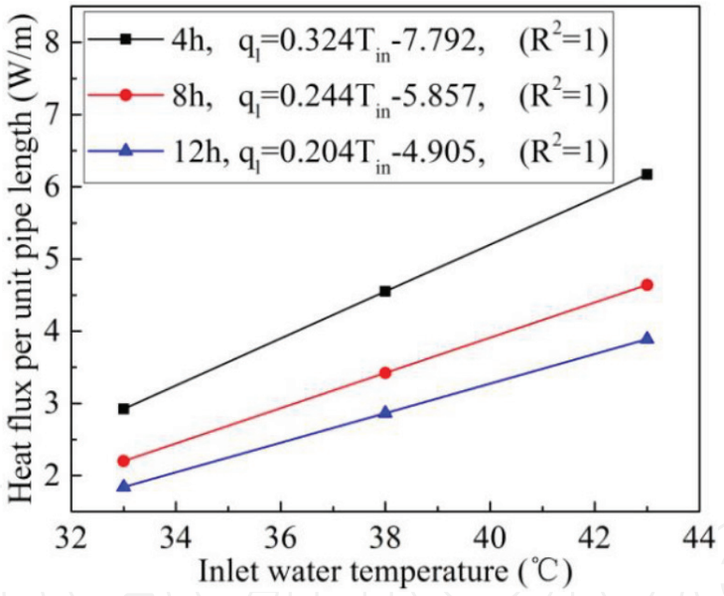

Figure 14. Heat flux per unit pipe length with various inlet water temperatures at different operation time.

fluxes per unit pipe length are 2.9, 2.2, and 1.83 W/m in the condition of the 33°C inlet water temperature. The heat fluxes per unit pipe length are 4.52, 3.42, and 2.83 W/m in the condition of 38°C inlet water temperature. Moreover, the heat fluxes per unit pipe length are 6.14, 4.64, and 3.87 W/m in the condition of 43°C inlet water temperature. The larger the inlet water temperature, the greater the heat flux per unit pipe length.

Figure 15 shows that with the increase of running time, the heat flux per unit pipe length decreases nonlinearly. And the fitting equations for three different inlet water temperature conditions are shown in the figure.

http://dx.doi.org/10.5772/intechopen.76821

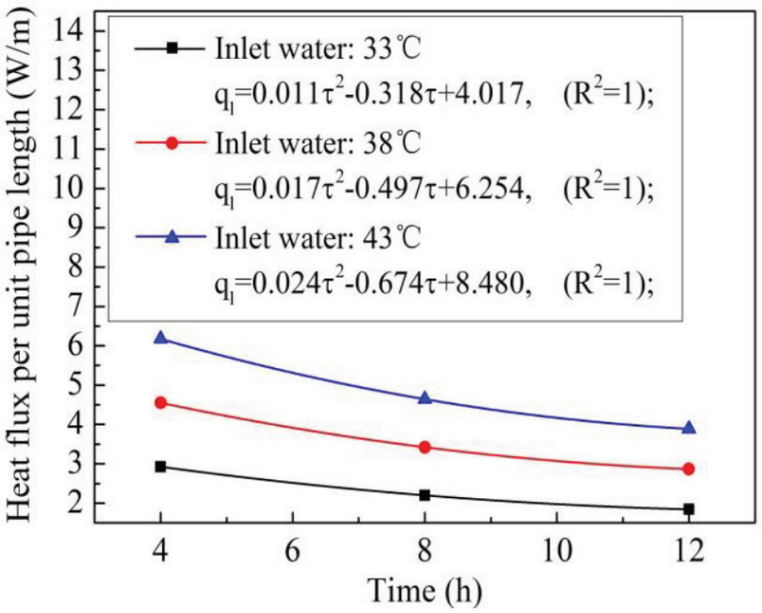

Figure 15. Heat flux per unit pipe length decreasing with operation time under different inlet water temperatures.

Figure 16 shows the fluid temperature distribution in the flow direction along the pipe length with the inlet water temperature of 33 38 and 43°C. It can be seen from the figure that the fluid temperature gradually decreases along the pipe length, and the fluid temperature reduction is more obvious in the entrance and exit stages of the CoHEP. **Figure 17** shows the heat flux per unit pipe length in the flow direction along the pipe length with the inlet water temperature of 33, 38 and 43°C. According to the geometry of CoHEP, as shown in **Figure 17**, the whole pipe of CoHEP is divided into four stages along the flow direction of the pipe length:

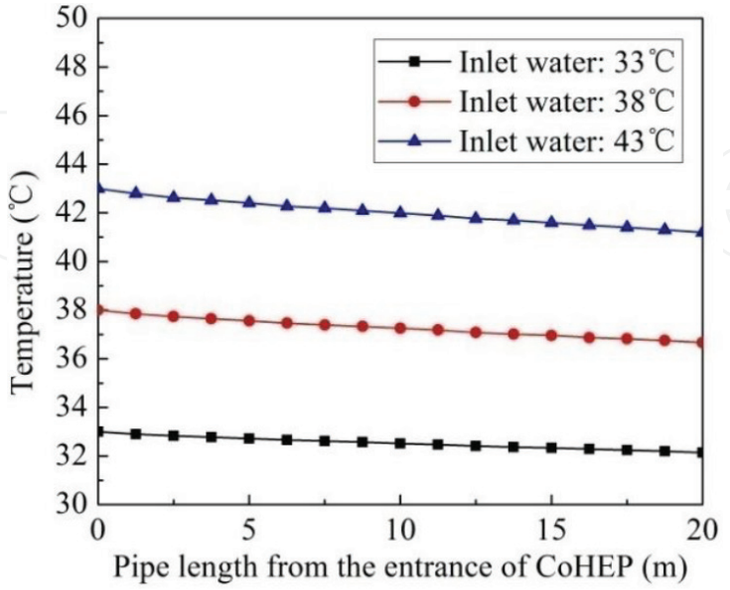

Figure 16. Water temperature distribution in the flow direction along the pipe length.

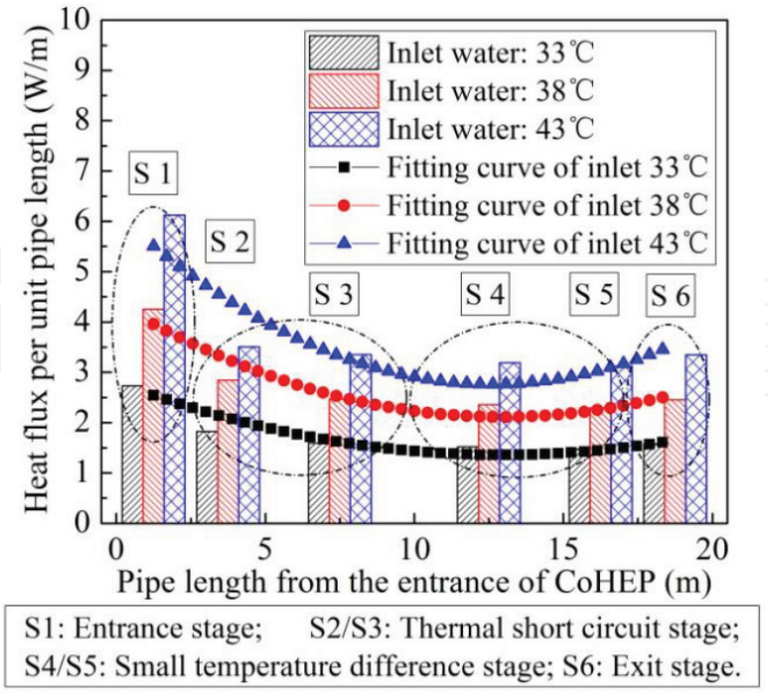

Figure 17. Heat flux per unit pipe length in the flow direction along the pipe length.

1. The entrance stage (S1): This stage is at the top of CoHEP which is in direct contact with the soil-covering area, and there is no heat transfer pipe in this area. Therefore, the heat transfer process in this stage has the following features: The fluid in this stage of the pipe not only radiates heat in the direction of diameter but also in the axial direction to the soil-covering area above the CoHEP, resulting in greater heat exchange capacity at this stage.

2. The thermal short circuit stage (S2 + S3): As the flow distance along the pipe length increases, the entrance stage ends. Due to the accumulation of heat in the soil, the thermal short circuit between the spiral pipes in the axial direction is serious, and the heat is mainly transferred in the diameter direction. Thus, the heat exchange capacity at this stage weakens.

3. The small temperature difference stage (S4 + S5): As the thermal short circuit stage ends, the fluid in the pipe decreases further, resulting in a decrease of the temperature difference between the fluid and the soil around. At the same time, due to the small diameter of the lower part of CoHEP, there is thermal short circuit both in the diameter direction and the in the axial direction. Therefore the heat exchange capacity reduces further at this stage.

4. The exit stage (S6): As the small temperature difference stage ends, the fluid is close to the exit of the pipe and this stage is defined as the exit stage. The exit stage is similar to the entrance stage. Since the pipe at the exit stage is in direct contact with the soil at the bottom of the buried CoHEP, the axial thermal short circuit effect is weak. The fluid in this stage of the pipe not only radiates heat in the direction of diameter but also in the axial direction to the soil at the bottom of the buried CoHEP. Thus, the heat exchange capacity increases at this stage.

3. Conclusions

A novel truncated cone helix energy pile (CoHEP) is presented to weaken the thermal interferences and improve the heat transfer efficiency. Further, both analytical solution model and numerical solution model for CoHEP are built to discuss their dynamic characteristics of thermal interferences and heat transfer performance. The following conclusions can be drawn.

1. Four heat exchange stages for the spiral pile geothermal heat exchanger along the fluid flow direction are revealed: inlet heat exchange stage, grout thermal short-circuiting stage, small temperature difference stage and outlet heat exchange stage. Each stage has corresponding heat transfer characteristics, and reducing the length of small temperature difference stage and increasing the other stages would enhance the heat exchange of the spiral geothermal ground heat exchanger.

2. The thermal interference of CoHEP is dynamic. When Fo < 1, the RTI of CyHEP is weaker than that of CoHEP in the bottom and the dimensionless temperature rise on the pile wall is lower than that of CoHEP. However, The GTI in the base of CoHEP is weaker than the other place of CoHEP and CyHEP, and the dimensionless temperature rise in the base of CoHEP is lower when Fo > 1.

Besides, the dimensionless temperature rise on the upper pile wall of CoHEP is lower than that of CyHEP when Fo < 5 and the RTI of CoHEP is weaker than that of CyHEP in the top of the pile. However, when Fo > 5, the temperature difference between CyHEP and CoHEP in the upper parts is nothing because the BTI tends to severe.

3. The thermal interference in the upper part of the CoHEP is much smaller than the traditional CyHEP. Moreover, under the same pitch in the depth direction (b) condition, the distance between the adjacent tube of CoHEP (d) is obviously larger than that of the traditional CyHEP, which can effectively reduce the axial thermal interference. Thus in general the heat flux per unit pipe length of the novel CoHEP is larger than that of the traditional CyHEP.

4. Heat flux per unit pipe length of the CoHEP increases linearly with the inlet water temperature. Thus the thermal performance of the CoHEP can be enhanced by increasing the inlet water temperature. But the inlet water temperature's increase will also lead to the increase of the outlet water temperature. It will cause a high condensation temperature and reduce the efficiency of the system. There is an optimal inlet water temperature, which needs to be analyzed together with the overall system's heat exchange efficiency.

For the same inlet water temperature, the thermal short circuit is serious at the bottom of the CoHEP, and it's weak in the upper part of the CoHEP. Also it's obvious that as the inlet water temperature increases, the thermal short circuit becomes more serious.

Acknowledgements

I would like to express my gratitude to all those who helped me during the writing of this book. And I feel grateful to all the teachers in the Army Logistical University of PLA who once

offered me valuable courses and advice during my study. Last, my thanks go to my beloved family for their loving considerations and great confidence in me all through these years. I also owe my sincere gratitude to my friends who gave me their help and time in listening to me and helping me work out my problems during the difficult course of the book.

This work received support from the Research Initiative for Basic Science and Frontier Technology of Chongqing, China [cstc2016jcyjA0496], Natural Science Foundation of China [51706243].

Conflict of interest

We declare that we have no financial and personal relationships with other people or organizations that can inappropriately influence our work; there is no professional or other personal interest of any nature or kind in any product, service, and/or company that could be construed as influencing the position presented in, or the review of, our work.

Nomenclature

x, y, z	Cartesian coordinate (m)
r, ϕ, z	cylindrical coordinate (m)
R,ϕ, Z	dimensionless cylindrical coordinate
h	height (m)
H	dimensionless height
r	radial coordinate (m)
R	dimensionless radial coordinate
q_{l}	heating rate per length of pipe (W s^{-1})
τ	the time (s)
α_{s}	thermal diffusivity (m^{-2} s)
d_{p}	distance from the heat source point to the calculated point (m)
d_{n}	distance from the heat sink point to the calculated point (m)
D_{p}	dimensionless distance from the heat source point to the calculated point (m)
D_{n}	dimensionless distance from the heat sink point to the calculated point (m)
ρ	density (kg m^{-3})
c	specific heat (J kg^{-1} K^{-1})

λ	thermal conductivity (W m^{-1} K^{-1})
$\triangle T$	the temperature rise (K)
R	thermal resistance (m^{-1} K^{-1} W)
L	length of helix pipe

Greek symbols.

θ	cone angle (rad)
ϕ	spiral angle (rad)
Fo	Fourier number
η	influence coefficient
Θ	dimensionless temperature rise

Superscript.

′	integration parameter
ave.	the average value
CyHEP	cylinder helix energy pile
CoHEP	truncated cone helix energy pile
t	top surface of pile
b	base surface of pile
mi	middle surface of pile
i	the index of arc
j	the index of coil
k, n	the index of time
p	pipe
f	fluid
g	ground

Author details

Guangqin Huang*, Yajiao Liu, Xiaofeng Yang and Chunlong Zhuang

*Address all correspondence to: hgq880818@163.com

Department of Military Installation, Army Logistical University of PLA, Chongqing, China

References

[1] Park S, Lee D, Choi H-J, Jung K, Choi H. Relative constructability and thermal performance of cast-in-place concrete energy pile: Coil-type GHEX (ground heat exchanger). Energy. 2015;**81**:56-66. DOI: 10.1016/j.energy.2014.08.012

[2] Park S, Sung C, Jung K, Sohn B, Chauchois A, Choi H. Constructability and heat exchange efficiency of large diameter cast-in-place energy piles with various configurations of heat exchange pipe. Applied Thermal Engineering. 2015;**90**:1061-1071. DOI: 10.1016/j.applthermaleng.2015.05.044

[3] Yang W, Lu P, Chen Y. Laboratory investigations of the thermal performance of an energy pile with spiral coil ground heat exchanger. Energy and Buildings. 2016;**128**:491-502. DOI: 10.1016/j.enbuild.2016.07.012

[4] Park SK, Lee S-R, Park H, Yoon S, Chung J. Characteristics of an analytical solution for a spiral coil type ground heat exchanger. Computers and Geotechnics. 2013;**49**:18-24. DOI: 10.1016/j.compgeo.2012.11.006

[5] Li M, Lai Alvin CK. Heat-source solutions to heat conduction in anisotropic media with application to pile and borehole ground heat exchangers. Applied Energy. 2012;**96**:451-458. DOI: 10.1016/j.apenergy.2012.02.084